Solution Structure of Human Mts1 (S100A4) As Determined by NMR Spectroscopy†

Kristen M. Vallely,‡ Richard R. Rustandi,‡ Karen C. Ellis,‡ Olga Varlamova,§ Anne R. Bresnick,*,§ and David J. Weber*,‡

Department of Biochemistry and Molecular Biology, University of Maryland School of Medicine, 108 North Greene Street, Baltimore, Maryland 21201, and Department of Biochemistry, Albert Einstein College of Medicine, 1300 Morris Park Avenue, Bronx, New York 10461

Received May 16, 2002; Revised Manuscript Received August 7, 2002

ABSTRACT: Mts1 is a member of the S100 family of Ca^{2+}-binding proteins and is implicated in promoting tumor progression and metastasis. To better understand the structure−function relationships of this protein and to begin characterizing its Ca^{2+}-dependent interaction with protein binding targets, the three-dimensional structure of mts1 was determined in the apo state by NMR spectroscopy. As with other S100 protein family members, mts1 is a symmetric homodimer held together by noncovalent interactions between two helices from each subunit (helices 1, 4, 1′, and 4′) to form an X-type four-helix bundle. Each subunit of mts1 has two EF-hand Ca^{2+}-binding domains: a pseudo-EF-hand (or S100-hand) and a typical EF-hand that are brought into proximity by a small two-stranded antiparallel β-sheet. The S100-hand is formed by helices 1 and 2, and is similar in conformation to other members of the S100 family. In the typical EF-hand, the position of helix 3 is similar to that of another member of the S100 protein family, calcyclin (S100A6), and less like that of other S100 family members for which three-dimensional structures are available in the calcium-free state (e.g., S100B and S100A1). The differences in the position of helix 3 in the apo state of these four S100 proteins are likely due to variations in the amino acid sequence in the C-terminus of helix 4 and in loop 2 (the hinge region) and could potentially be used to subclassify the S100 protein family.

Mts1, also known as S100A4, p9Ka, calvasculin, metastasin, 18A2, pEL98, and CAPL, belongs to the S100 family of Ca^{2+}-binding proteins (*1*−*4*). S100 proteins are small (10−12 kDa per subunit), acidic proteins that are characterized by their solubility in 100% ammonium sulfate (*5*). There are currently 21 known S100 family members (Figure 1), most of which are expressed in a highly tissue specific manner (*1*, *3*, *6*). While mts1 is expressed in a wide range of normal tissues (*1*), high expression levels correlate with the metastatic potential of tumor cells. For example, metastatic rat and mouse mammary tumor cells contain higher levels of mts1 than nonmetastatic cells (*7*), and the level of mts1 expression is higher in malignant human breast tumors than in benign tumors (*8*), which correlates strongly with poor patient survival (*9*, *10*). Furthermore, overexpression of mts1 in nonmetastatic rat and mouse mammary tumor cells confers a metastatic phenotype, whereas in metastatic cells, a reduction in the level of mts1 expression suppresses metastasis (*11*, *12*). In transgenic mouse models of breast cancer, overexpression of mts1 in murine mammary tumor virus-induced (*13*) or in *neu* oncogene-induced (*14*) benign mammary tumors induces lung metastasis. These findings directly implicate mts1 in the establishment of the metastatic phenotype.

As with other S100 family members, mts1 activity is regulated by intracellular calcium ion concentrations. Mts1 displays Ca^{2+}-dependent interactions with target proteins that include the p53 tumor suppressor protein, non-muscle myosin II, tropomyosin, and F-actin, which may be related to its role in cancer and metastasis (*15*−*18*). This Ca^{2+}-dependent regulation occurs in mts1 via two helix−loop−helix Ca^{2+}-binding domains known as EF-hands (*19*). As with other S100 proteins, the C-terminal binding domain of mts1 (typical EF-hand) contains 12 residues and binds calcium with a higher affinity (K_d < 50 μM) than the N-terminal domain (pseudo-EF-hand or S100-hand), which contains 14 residues (K_d > 50 μM) (*20*, *21*). Structural studies of several S100 proteins (i.e., S100B, S100A1, and calcyclin) indicate that the orientation of helix 3 in the typical EF-hand changes upon calcium binding (*22*−*25*). However, the magnitude of the conformational change differs among the S100 proteins due to variations in the position of helix 3 in the apo state (*23*, *25*). For example, helix 3 of S100B undergoes a very large conformational change when going from the apo to the calcium-bound state, whereas the change in the orienta-

† This work was supported by the National Institutes of Health (Grant GM58888 to D.J.W.), the American Cancer Society (Grant RPG0004001-CCG to D.J.W.), and the Department of Defense Breast Cancer Research Program (Grant DAMD17-01-1-0122 to A.R.B.). This work also made use of the UMB NMR facility that was supported by the Shared Instrumentation Grant Program (Grants RR10441, RR15741, and RR16812 to D.J.W.).

* To whom correspondence should be addressed. D.J.W.: telephone, (410) 706-4354; fax, (410) 706-0458; e-mail, dweber@umaryland.edu. A.R.B.: telephone, (718) 430-2741; fax, (718) 430-8565; e-mail, bresnick@aecom.yu.edu.

‡ University of Maryland School of Medicine.

§ Albert Einstein College of Medicine.

10.1021/bi020365r CCC: $22.00
Published on Web 09/27/2002

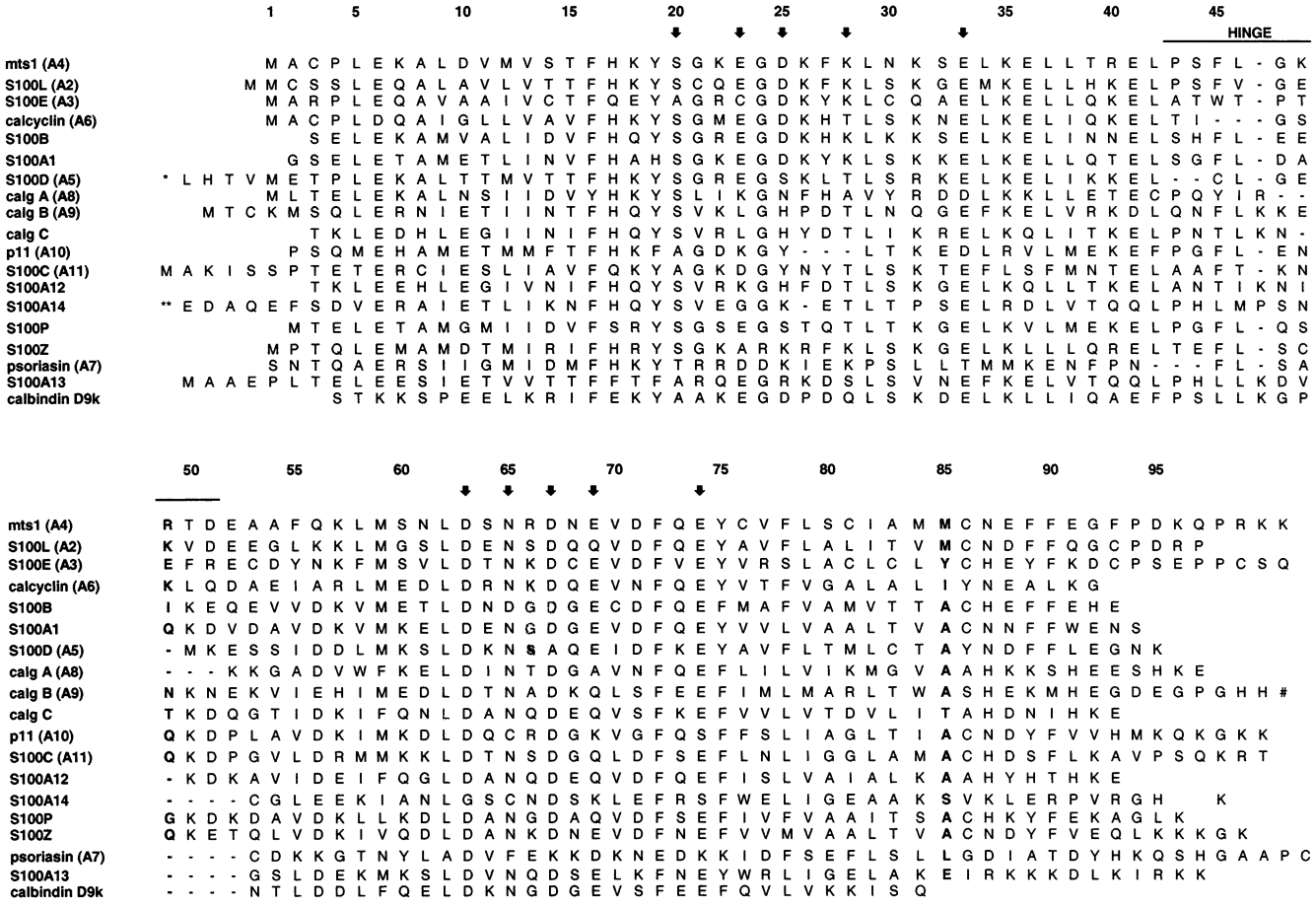

FIGURE 1: Amino acid sequence alignment of members of the S100 protein family. The sequence numbering is based on human mts1. The highlighted region shows the "hinge" (loop 2) of the proteins. The residues shown in bold (positions 49 and 85 of mts1) were used to identify the putative subfamilies of S100 proteins. Residues that coordinate calcium are denoted with arrows at the *X*, *Y*, *Z*, $-Y$, $-X$, and $-Z$ sites. The first 15 residues of S100D are MPAAWILWAHSHSE and are denoted with an asterisk; the first nine residues of S100A14 are MGQCRSANA and are denoted with a double asterisk, and the final 10 residues of calgranulin B are HKPGLGEGTP and are denoted with the number symbol.

tion of helix 3 in calcyclin is less pronounced (*22*−*26*). These types of conformational variations may be important indicators of functional differences between members of the S100 protein family.

Mts1 binds its protein targets in a Ca^{2+}-dependent manner and is likely to undergo a conformational change in the typical EF-hand upon binding calcium as observed for other S100 proteins (*26*). To characterize this conformational change, it is necessary to determine the three-dimensional (3D) structure of mts1 both in the presence and in the absence of calcium. As an initial step in this process, we have determined the solution structure of apo-mts1 using heteronuclear multidimensional NMR. The topological fold of apo-mts1 is similar to that of other S100 family members, consisting of a homodimer held together at the dimer interface by an X-type four-helix bundle. In addition, the orientation of helix 3 in apo-mts1 is similar to that of helix 3 in apocalcyclin (*23*), and is less like that of apo-S100B (*25*) and apo-S100A1 (*27*).

MATERIALS AND METHODS

Bacterial Expression and Purification of Mts1. For the production of the untagged protein, human mts1 was subcloned into the *Nde*I and *Bam*HI sites of the expression vector pET3a (Novagen). For the purification of ^{15}N-labeled or ^{13}C- and ^{15}N-labeled mts1, BL21(DE3) cells were transformed with hmts1-pET3a and cultures were grown in minimal medium using [^{15}N]ammonium sulfate and/or [$^{13}C_6$]-glucose (Martek Biosciences Corp.) as the sole nitrogen and carbon sources, respectively. Cells were grown at 37 °C to an OD_{600} of 0.8 and induced with 1 mM IPTG[1] overnight. For unlabeled mts1, cultures were grown in Luria broth (LB) and induced using 1 mM IPTG. The cells were harvested at 15000*g*, and the cell pellet was resuspended in 10 mL of lysis buffer [50 mM Tris (pH 7.5), 10% glycerol, 300 mM KCl, 2 mM DTT, 1 mM EDTA, 1 mM PMSF, 5 μg/mL chymostatin, 5 μg/mL leupeptin, and 5 μg/mL pepstatin] per gram of cell pellet. The cell lysate was frozen, thawed on ice, and sonicated. Following centrifugation of the lysate at 100000*g* for 30 min, ammonium sulfate was added to the supernatant to 30% saturation and the sample centrifuged at 17000*g* for 20 min. $CaCl_2$ was added to the supernatant to a final concentration of 2 mM, and the sample was applied to a Phenyl-Sepharose column (Pharmacia) equilibrated in buffer P [20 mM Tris (pH 7.5), 2 mM $CaCl_2$, 300 mM KCl,

[1] Abbreviations: IPTG, isopropyl β-D-thiogalactopyranoside; DTT, dithiothreitol; rmsd, root-mean-square deviation; NOE, nuclear Overhauser effect; NMR, nuclear magnetic resonance; HSQC, heteronuclear single-quantum coherence; TPPI, time-proportional phase incrementation; 3D, three-dimensional.

1 mM DTT, and 1 mM EDTA] containing 16.4 g of ammonium sulfate/100 mL. The column was washed with 3 column volumes of buffer P containing 16.4 g of ammonium sulfate/100 mL and then with 3 column volumes of buffer P without ammonium sulfate, and mts1 eluted with 20 mM Tris (pH 7.5), 5 mM EGTA, 1 mM DTT, and 1 mM EDTA. Fractions containing mts1 were pooled and dialyzed against 4.0 L of buffer D [20 mM Tris (pH 7.5), 0.2 mM DTT, and 0.02% NaN_3]. The dialyzed pool was applied to a Fast Q column (Pharmacia) and the column washed with 4 column volumes of buffer D. Mts1 eluted in the flow through and was pooled and dialyzed against 20 mM Tris (pH 7.5), 50 mM NaCl, 1 mM DTT, and 0.02% NaN_3. Typical protein yields were 5 mg of mts1 per liter of cells. Gel filtration chromatography of the purified mts1 in the presence of a reducing agent was consistent with this protein forming a noncovalent dimer as found for other S100 proteins (*28*).

NMR Spectroscopy. Purified mts1 was dialyzed against 0.1 mM Tris-d_{11} (pH 7.5) and 0.1 mM DTT, lyophilized, hydrated in a small aliquot of ddH_2O, and stored at −80 °C. The final NMR samples contained 2−3 mM mts1 monomer, 0.34 mM NaN_3, 8 mM NaCl, 16 mM Tris-d_{11}, 0.2 mM EDTA, 2 mM EGTA, 6 mM DTT, and 7% D_2O. In all samples, the pH was adjusted with cold HCl to 6.5. In the Ca^{2+}−mts1 sample, the conditions were as for the apo-mts1 samples, except 10 mM $CaCl_2$ was added and EGTA was excluded. Ca^{2+} was titrated in 2 mM increments; the pH was adjusted to 6.5, and a $^1H-^{15}N$ HSQC spectrum was collected after each addition. Prior to use, stock solutions of all buffer components were passed through a Chelex-100 column to remove any trace metals.

NMR data were collected at 37 °C with a Bruker DMX600 NMR spectrometer (600.13 MHz for protons) equipped with pulsed-field gradients, four frequency channels, and a triple-resonance, triple-axis gradient probe. Unless otherwise stated, a 1 s relaxation delay was used and quadrature detection in the indirect dimensions was obtained with States−TPPI phase cycling (*29*). For most experiments, initial delays in the indirect dimensions were set to give zero- and first-order phase corrections of 90° and −180°, respectively (*30*). Data were processed on Silicon Graphics workstations using the processing program NMRPipe (*31*). Time domain data in the indirect dimensions were extended by no more than one-third using standard linear prediction routines (*32*), except for data in constant time domains that were extended 2-fold using mirror-image linear prediction (*33*). All proton chemical shifts are reported with respect to the H_2O or HDO signal taken to be 4.658 ppm relative to external TSP (0.0 ppm) at 37 °C. The ^{13}C and ^{15}N chemical shifts were indirectly referenced using the following ratios of the zero-point frequencies at 37 °C: 0.10132905 for $^{15}N-^1H$ and 0.25144953 for $^{13}C-^1H$ (*34*−*36*).

Unlabeled mts1 in D_2O (>99%) was used to record two-dimensional (2D) NOESY (*37*) and TOCSY (*38*) experiments. Uniformly ^{15}N-labeled mts1 was used to collect the 2D $^1H-^{15}N$ fast HSQC spectra (*39*), the 3D ^{15}N-edited NOESY-HSQC spectra (*40*) with a mixing time of 100 ms, the 3D ^{15}N-edited HOHAHA-HSQC spectra with a spin-lock time of 60 ms using a 10 kHz rf field strength and a DPSI-2rc mixing sequence (*38*, *41*, *42*), the 3D ^{15}N-edited HMQC-NOESY-HMQC spectra (*43*) with a mixing time of 125 ms, and the 3D HNHA spectra (*44*, *45*) for measuring $^3J_{NH-H\alpha}$ coupling constants. A uniformly ^{13}C- and ^{15}N-labeled apo-mts1 sample was used to collect the 3D C(CO)NH spectra (*46*, *47*), the 3D CBCA(CO)NH spectra (*46*, *48*), the 3D HNCACB spectra (*49*), the sensitivity-enhanced 4D ^{13}C, ^{15}N-edited NOESY-HSQC spectra (*50*) with a mixing time of 100 ms, and the 4D ^{13}C, ^{13}C-edited NOESY-HSQC spectra (*44*) with a mixing time of 100 ms. In all of the ^{15}N-edited experiments, the fast-HSQC detection scheme was incorporated into the sequence to avoid water saturation. Pulsed field gradients were used throughout the NMR pulse sequences as needed to purge undesired magnetization (*51*).

NMR-Derived Constraints and Structure Calculations. Interproton distance constraints derived from NOE cross-peaks were classified into five categories (strong, medium, medium weak, weak, and very weak) and then assigned distance constraints with lower bounds of 1.8 Å and upper bounds of 2.7 (2.9 Å for HN), 3.3 (3.5 Å for HN), 4.2, 5.0, and 6.0 Å, respectively (*52*). Pseudoatom corrections were added to the upper limit for degenerate methyl, methylene, and aromatic ring protons (*53*, *54*), and constraints for methyl protons were shifted down by one category as previously described (*53*, *55*). Because only structurally useful NOE correlations were used, NOE correlations between geminal protons and between vicinal methylene protons were excluded. Constraints derived from weak or very weak NOE correlations were used only when reciprocal NOE correlations of similar intensities were observed. Dihedral constraints of $\phi \pm 20°$ and $\psi \pm 15°$ for α-helices and $\phi \pm 40°$ and $\psi \pm 40°$ for β-sheets were included on the basis of hydrogen exchange rates, $^3J_{NH-H\alpha}$ coupling constants, and chemical shift indices of $^1H^\alpha$ and $^{13}C^\alpha$ (*56*). In the final stage of structure determination, the following backbone hydrogen bond constraints were included in regions of secondary structure: $r_{NH-O} = 1.5-2.8$ Å and $r_{N-O} = 2.4-3.5$ Å.

Structures were calculated using X-PLOR version 3.851 (*57*) using the standard protocols for substructure embedding and regularization, hybrid distance geometry-simulated annealing (DGSA) regularization and refinement, and simulated annealing (SA) refinement (*58*−*60*). Noncrystallographic symmetry (NCS) and distance symmetry constraints with force constants of 100 and 1 kcal mol^{-1} $Å^{-2}$, respectively, were employed using DGSA and SA routines to preserve the symmetry of the mts1 homodimer (*61*). A conformational database potential and pseudopotentials for secondary $^{13}C^\alpha$ and $^{13}C^\beta$ chemical shifts were included in the SA refinement (*62*, *63*). The refinement procedure yielded several (>50) structures with no distance violations of greater than 0.4 Å and no dihedral constraint violations of greater than 5°. The final 20 structures were chosen on the basis of having the lowest total energies. Table 1 includes statistics for this family of low-energy structures, and their coordinates have been deposited in the Protein Data Bank (PDB) as entry 1M31.

Structure Calculations for the Homology Model of Ca^{2+}-Bound Mts1. A homology model of the non-hydrogen atoms of the Ca^{2+}-loaded structure of mts1 was calculated using comparative structure modeling methods that satisfy spatial restraints with the computer program MODELLER (*64*−*66*). Templates for this calculation included Ca^{2+}-loaded structures of rat S100B (PDB entry 1QLK), rabbit calcyclin (PDB entry 1A03), and human psoriasin (PDB entry 3PSR),

Table 1: NMR-Derived Restraints and Statistics of NMR Structures[a]

	⟨20⟩	best
rmsd from distance constraints (Å)[b]		
total (2222)	0.045 ± 0.0015	0.047
intraresidue (554)	0.013 ± 0.0014	0.011
sequential ($\|i - j\| = 1$) (660)	0.032 ± 0.0034	0.033
medium-range ($1 < \|i - j\| \leq 5$) (616)	0.071 ± 0.0023	0.073
long-range ($\|i - j\| > 5$) (188)	0.058 ± 0.0076	0.068
intermolecular for dimer interface (70)	0.019 ± 0.0073	0.018
intra- and/or intermolecular (18)	0.018 ± 0.017	0.000
hydrogen bonds (116)	0.013 ± 0.0037	0.009
rmsd from exptl dihedral restraints[b]		
ϕ and ψ (250)	0.4693 ± 0.078	0.4124
rmsd from exptl ^{13}C chemical shifts		
$^{13}C\alpha$ (ppm)	1.236 ± 0.035	1.259
$^{13}C\beta$ (ppm)	0.904 ± 0.038	0.883
rmsd from idealized covalent geometry		
bonds (Å)	0.0043 ± 0.00014	0.0044
angles (deg)	0.562 ± 0.014	0.549
impropers (deg)	0.500 ± 0.037	0.441
Lennard-Jones potential energy (kcal/mol)[c]	−797.06 ± 32.54	−818.03
% of residues in the most favorable region of the Ramachandran plot[d]	85.5	86.8
rmsd to the mean structure (Å)		
all backbone atoms in secondary structure[e]	0.158 ± 0.0516	0.136
all ordered heavy atoms in mts1[e]	0.988 ± 0.1614	1.006
all backbone atoms in mts1 (4−86)[f]	0.878 ± 0.0924	0.864
all heavy atoms in mts1 (4−86)[f]	1.609 ± 0.0947	1.610

[a] The ensemble of 20 structures, ⟨20⟩, are the result of simulated annealing (SA) calculations. The best of the group was chosen on the basis of having the lowest overall energy. For ⟨20⟩, the values shown are the means ± the standard deviation. [b] The force constants used in the refinement are as follows: 1000 kcal mol^{-1} Å^{-2} for bond length, 500 kcal mol^{-1} rad^{-2} for angles and improper torsions, 4 kcal mol^{-1} Å^{-4} for the quartic van der Waals (vdw) repulsion term (hard-sphere effective vdw radii set to 0.8 times their values in CHARMm parameters), 50 kcal mol^{-1} Å^{-2} for experimental distance restraints, 150 kcal mol^{-1} rad^{-2} for dihedral constraints, 100 kcal mol^{-1} Å^{-2} for noncrystallographic symmetry, 1 kcal mol^{-1} Å^{-2} for distance symmetry constraints, 0.5 kcal mol^{-1} ppm^{-2} for ^{13}C chemical shift constraints, and 1.0 for conformational database potential. None of the 20 structures has a distance violation of >0.4 Å or a dihedral angle violation of >5°. [c] The Lennard-Jones van der Waals energy was calculated using CHARMm parameters and was not used in any stage of the structure determination. [d] PROCHECK was used to determine the Ramachandran plot. [e] The calculation included the backbone atoms (C_α, N, and C′) in the four helices and the two β-strands per subunit (E6−Y19, K28−N30, K31−R40, A54−D63, E69−D71, and F72−C86). [f] The calculation included all backbone residues excluding the unassigned N-terminal residues and the unstructured C-terminal tail region, due to the lack of NOE correlations in both regions (only *one* long-range NOE is present in the entire stretch of residues N87−K101). Also, the high rmsd value that is obtained is a reflection of a lack of observable NOE correlations in the exchange-broadened hinge region.

and the lowest-energy NMR structure of apo-mts1 was used as a starting point in the holo-mts1 model calculation. The preliminary alignment of mts1 with holo-S100B, holocalcyclin, and holopsoriasin was constructed solely on the basis of the sequences of the proteins such that the residues involved in the typical EF-hand and the pseudo-EF hand were in-frame. Next, a comparison of the three-dimensional structures of holo-S100B, holocalcyclin, and holopsoriasin was used to further refine the alignment such that the residues involved in helices 1 and 4 of the three templates were aligned in three-dimensional space with those in mts1. The sequence alignment in the variable loop region and the C-terminal insertion of mts1 contained no sequence identity, so no homology-derived constraints were created for these regions of mts1. Instead, this loop was modeled on the basis of the amino acid sequence in the context of the rest of the protein as previously described (*64*, *65*). Once mts1 was homology modeled on the basis of these three holo-S100 proteins, inclusion of hydrogen atoms and four Ca^{2+} ions was achieved using the program X-PLOR (*67*) as described previously for the determination of the solution structure of holo-S100B (*24*).

RESULTS AND DISCUSSION

Three-Dimensional Structure of Mts1. In total, the structure of apo-mts1 was calculated using a total of 2472 constraints, including 554 intraresidue, 660 sequential, 616 medium-range, 188 long-range, 70 intermolecular, 18 inter- or intramolecular NOE correlation, 116 hydrogen bond, and 250 dihedral angle constraints (ϕ and ψ; Table 1). NOE correlations were assigned on the basis of the previously reported ^{1}H, ^{13}C, and ^{15}N backbone and side chain chemical shift assignments for apo-mts1 (*68*) and indicated that apo-mts1 contains four α-helices and a small antiparallel β-sheet consistent with the presence of two helix−loop−helix Ca^{2+}-binding domains (Figure 2). Early on in the structure determination, it was clear that mts1 is a symmetric homodimer like that of other S100 proteins (*26*). For example, as illustrated in Figure 3, data from the four-dimensional (4D) ^{13}C, ^{13}C-edited NOESY experiment allowed for unambiguous NOE assignments from H_δ of L5 in helix 1 to $M12_\epsilon$, $M12_\beta$, and $V11_\gamma$ of helix 1′. These NOE correlations are not intramolecular since it is physically impossible for the opposite ends of helix 1 to be close enough to generate observable NOE correlations. Similarly, NOE correlations were assigned between the protons in helix 4 and helix 4′, indicating that these helices were oriented in an antiparallel manner. These and other unambiguous intermolecular NOE correlations defined the overall fold of the dimer interface of apo-mts1 as an X-type four-helix bundle. In total, 70 unambiguous intermolecular NOE constraints defined the dimer interface, involving residues in helix 1 (P4, L5, E6,

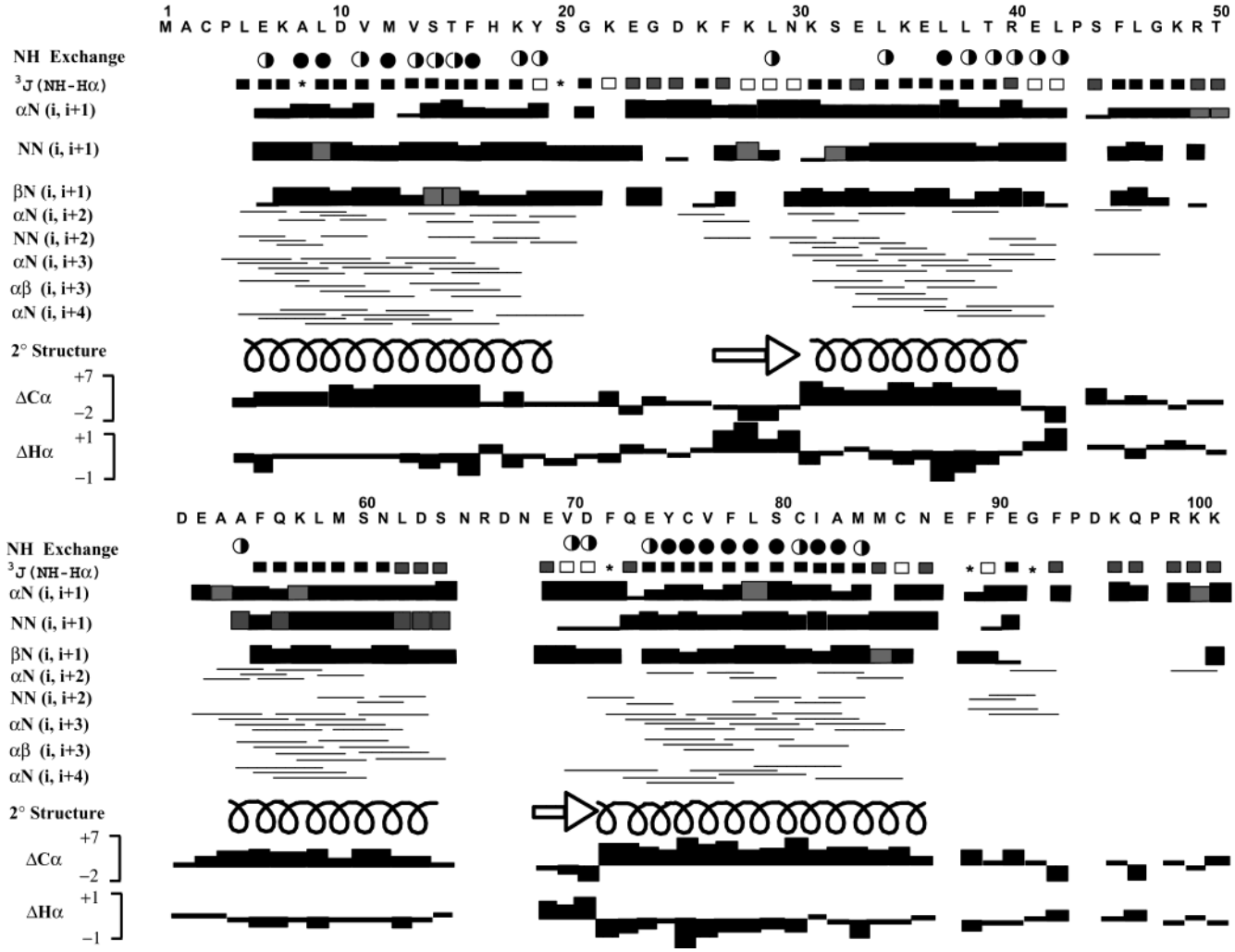

FIGURE 2: Diagram of amide exchange, NOE correlations, sequential correlations, and secondary structure for apo-mts1. Circles represent relative amide hydrogen exchange rates at 37 °C. Residues lacking a symbol (T < 0.25 h) are arbitrarily termed fast exchanging amide protons. Residues with half-shaded circles (0.25 h < T < 18 h) are termed medium exchanging amide protons. Residues with solid circles (T > 18 h) are termed slowly exchanging amide protons. J coupling values are as follows. Residues with gray boxes have values between 6 and 7.9 Hz. Residues with black boxes have values of <6 Hz. Residues with white boxes have values of >7.9 Hz. Residues with an asterisk were ambiguous due to overlap. 3D ^{15}N-edited NOESY-HSQC, 3D ^{15}N, ^{15}N-edited HMQC-NOESY-HMQC, and 4D ^{13}C, ^{15}N-edited NOESY experiments were conducted at 37 °C, as described in Materials and Methods to determine NOE correlations. The NOE strength is indicated by bar height (strong, medium, medium weak, weak, or very weak), and shaded boxes indicate tentative NOE strengths due to chemical shift overlap. $^{13}C^{\alpha}$ and $^{1}H^{\alpha}$ chemical shift deviations from random coil values are shown such that regions of upfield-shifted $^{13}C^{\alpha}$ chemical shifts (positive) and downfield-shifted $^{1}H^{\alpha}$ chemical shifts (negative) are indicative of helical regions. Similarly, regions of downfield-shifted $^{13}C^{\alpha}$ chemical shifts (negative) and upfield-shifted $^{1}H^{\alpha}$ chemical shifts (positive) are indicative of β-sheet regions (*56*, *80*−*82*). Secondary structure is represented by spirals for α-helices, arrows for β-strands, and no symbol for loops, as indicated under the appropriate residues in the mts1 sequence.

A8, L9, V11, M12, T15, and F16), helix 2 (L38), loop 3 (L42), helix 4 (F72, Q73, V77, L79, S80, and A83), and loop 5 (F89). Not surprisingly, many of the intermolecular NOE correlations derived from these residues in apo-mts1 are similar to NOE correlations observed at the dimer interface of both apo-S100A1 (E3, L4, E5, A7, M8, L11, V14, and F15 in helix 1, L41 in loop 2, Q72, V76, V78, A79, and T82 in helix 4, and F88 in loop 4) and apo-S100B (E2, L3, E4, A6, M7, A9, L10, V13, and F14 in helix 1, I36 in helix 2, S41 in loop 2, F70, Q71, A75, V77, and T81 in helix 4, and F87 in loop 4).

Figure 4 shows the superposition of the 20 lowest-energy structures that best fit the input data. These structures contain no NOE violations greater than 0.4 Å, no dihedral violations exceeding 5°, or hydrogen bond violations (Table 1). In addition, the 20 lowest-energy structures were found to have reasonable rmsd values when calculated from the average structure (<0.88 Å for backbone atoms and <1.61 Å for all atoms; Table 1) and very low rmsd values when only regions of secondary structure were considered (<0.16 Å; Table 1). The higher rmsd values observed in the loop regions are due primarily to the lack of structural constraints. This is especially pronounced in the second calcium-binding loop (N65−N68) and the C-terminal loop (N87−K101) of mts1. The lowest-energy structure (Figure 5) has good values in all of the categories presented in Table 1, and the majority of its residues are in the most favored region of the Ramachandran diagram (86.8%), with no residues in the disallowed regions. The quality of the 20 apo-mts1 structures was evaluated using the program PROCHECK (*69*) and is comparable to that of a 2 Å X-ray crystal structure.

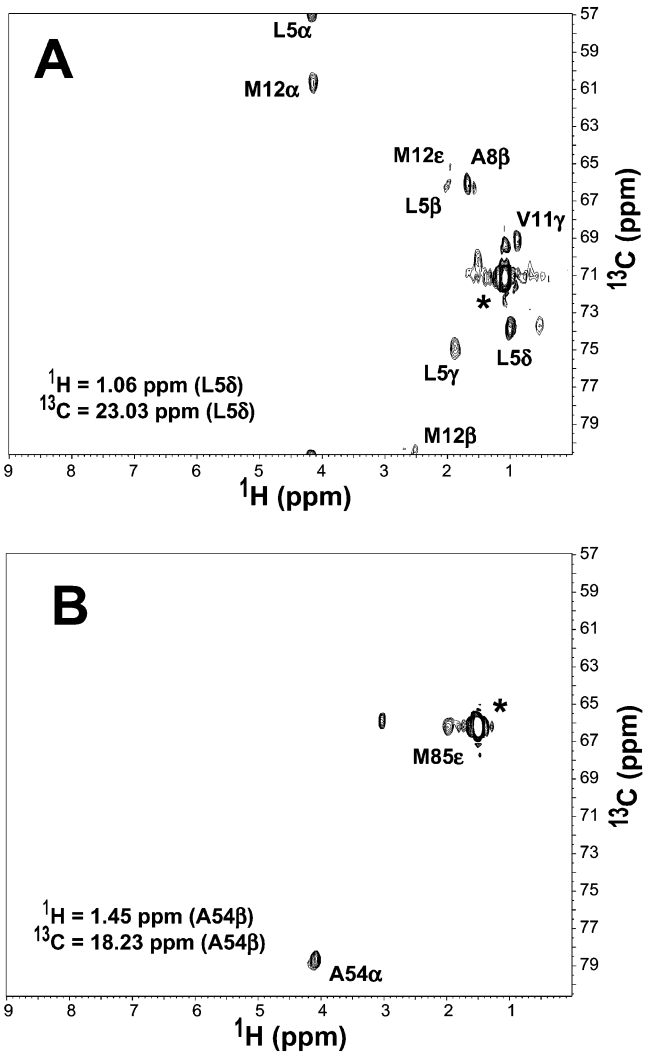

FIGURE 3: NOE data for apo-mts1. (A) Spectral plane from a 4D ^{13}C, ^{13}C-edited NOESY experiment illustrating intermolecular NOE correlations from L5δ (in helix 1) to M12 and V11 (helix 1′) at the dimer interface of apo-mts1 and (B) a plane from the same 4D ^{13}C, ^{13}C-edited NOESY experiment illustrating an NOE correlation between A54β of helix 3 and M85ϵ of helix 4. Unlabeled contours have their maximum intensities in other planes, and autocorrelation peaks are denoted with asterisks in each panel. As a result of spectral folding, chemical shift values on the *Y*-axis for carbon can be off by multiples of the sweep width in that dimension (i.e., 24 or 48 ppm).

The three-dimensional structures for three other dimeric S100 family members have been determined in the apo state, including S100B, calcyclin, and S100A1 (*23*, *25*, *27*). As found for these S100 proteins, each subunit of apo-mts1 has two EF-hand Ca^{2+}-binding domains brought into proximity via a short antiparallel β-sheet (K28−N30 in β1 and E69−D71 in β2). The overall fold of each subunit is that of a unicornate-type four-helix bundle (*70*) that interacts with its symmetric subunit via an X-type four-helix bundle comprising helices 1, 1′, 4, and 4′ (Figure 5). The N-terminal EF-hand in mts1 is termed a pseudo-EF-hand since its binding loop contains 14 residues, as opposed to 12 residues, as is found for typical EF-hand Ca^{2+}-binding domains (*19*). The pseudo-EF-hand domain of mts1 consists of helix 1 (residues E6−Y19), loop 2 (residues S20−K26), and helix 2 (residues K31−R40). The C-terminal EF-hand in mts1 is more typical, with a 12-residue EF-hand consensus sequence. It is comprised of helix 3 (residues A54−D63), loop 4 (residues S64−C68), and helix 4 (residues F72−C86). The two EF-hands are connected by a loop region (residues E41−A53) termed the hinge region, and the C-terminal EF-hand is followed by a lengthy C-terminal tail (N87−K101). Residues in the hinge and the C-terminal tail exhibit a minimal degree of, if any, sequence homology with the corresponding regions of other S100 protein family members (Figure 1), and it is these loops in mts1 that are likely responsible for conferring binding specificity to its protein targets.

Comparison of the Apo-Mts1 Structure to Other S100 Proteins. A common feature in all of the apo-S100 protein structures determined thus far is that the pseudo-EF-hand formed by helices 1 and 2 adopts a similar conformation both in the presence and in the absence of calcium (*26*), so it is not surprising that the corresponding interhelical angle in apo-mts1 is very similar ($\Omega^{I/II} = 119 \pm 2°$; Table 2) to those of apo-S100B, apo-S100A1, and apocalcyclin, which have $\Omega^{I/II}$ interhelical angles of 133°, 120°, and 126°, respectively. Likewise, the values for θ and ϕ of the pseudo-EF-hand (Table 3) of apo-mts1 are similar to those of apocalcyclin, apo-S100B, and S100A1 when using the vector geometry method (VGM) to evaluate helical angles. Therefore, as for other S100 proteins, the pseudo-EF-hand of mts1 probably does not play a role in the calcium-induced conformational change required for target protein binding (*26*). Another similarity in the apo-mts1 three-dimensional structure is that the X-type four-helix bundle that comprises the dimeric fold of apo-mts1 is like that of other apo-S100 proteins. This is clearly evident when the helix 1−helix 4 ($\Omega^{I/IV}$), helix 1−helix 1′ ($\Omega^{I/I'}$), and helix 4−helix 4′ ($\Omega^{IV/IV'}$) interhelical angles for apo-mts1 are compared to those of other S100 proteins (Table 2).

The significant difference between the structures of various S100 proteins in the apo state is the position of helix 3 relative to helices 1, 2, and 4 (Figure 6 and Tables 2 and 3). For example, the interhelical angle between helices 3 and 4 ($\Omega^{III/IV}$) is $-166 \pm 1°$ in apo-S100B and $-150 \pm 1°$ in apo-S100A1, whereas the same angle in apocalcyclin differs significantly ($\Omega^{III/IV} = 150 \pm 2°$; Table 2). In apo-mts1, the interhelical angle of helices 3 and 4 is $162 \pm 4°$, which more closely resembles that of apo-alcyclin (Table 2). Likewise, results from vector geometry mapping lead to a similar conclusion (Table 3) (*71*). This can be observed most directly by comparing the ϕ angles, which are $-43 \pm 13°$ and $-62 \pm 4°$ for apo-mts1 and apocalcyclin, respectively, whereas ϕ equals $-120 \pm 4°$ and $-85 \pm 7°$ for the typical EF-hands of apo-S100B and apo-S100A1, respectively (Table 3). Together, these data suggest that there are two subfamilies of S100 proteins that display differences with respect to the positioning of helix 3 relative to helix 4 in the apo state. To date, it is proposed that one subfamily should include S100B and S100A1 ($-170° < \Omega^{III/IV} < -150°$; $-120° < \phi < -80°$) and the other subfamily should include mts1 and calcyclin ($150° < \Omega^{III/IV} < 170°$; $-70° < \phi < -30°$; Figures 6 and 7).

Close examination of the three-dimensional structures of apo-mts1, apocalcyclin, apo-S100B, and apo-S100A1 reveals specific differences in sequence and side chain packing for residues in the hinge and C-terminus of helix 4. These differences are likely the reason for the variation observed in the orientation of helix 3 with respect to helix 4 in the

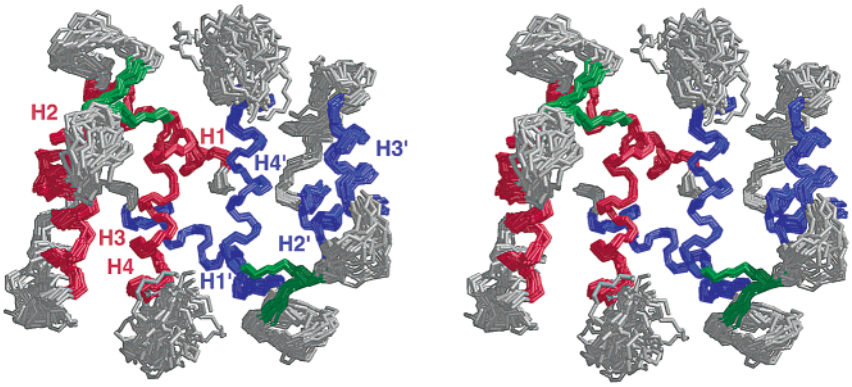

FIGURE 4: Stereoview of the overlay of the 20 low-energy structures of apo-mts1 based on NMR-derived constraints. The helices are shown in red for one subunit and in blue for the other subunit. The β-strands are colored green for both subunits. Listed in Table 2 are the statistics for this family of structures.

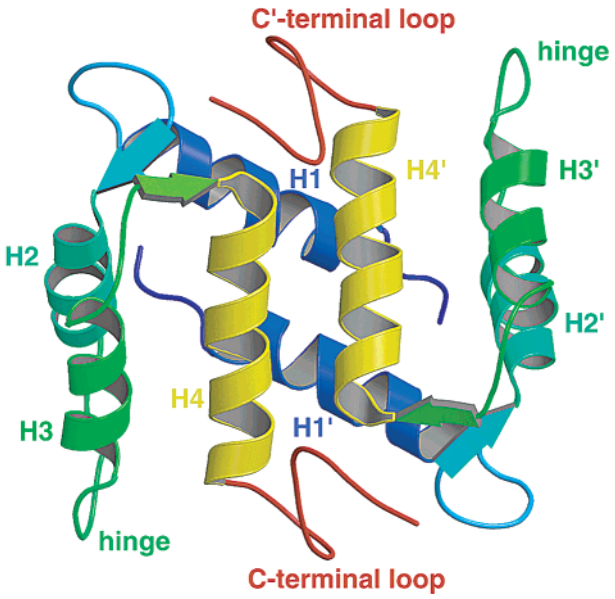

FIGURE 5: Ribbon diagram of apo-mts1. Helices H1 and H1′ (blue), H2 and H2′ (teal blue), H3 and H3′ (green), and H4 and H4′ (yellow) form an X-type four-helix bundle at the dimer interface in apo-mts1 (*70*).

Table 2: Interhelical Angles of S100 Proteins[a]

helices	apo-mts1[b]	apocalcyclin[b,c]	apo-S100B[b,d]	apo-S100A1[b,e]
I−II	119 ± 2	126 ± 2	133 ± 1	120 ± 3
I−III	−55 ± 4	−52 ± 2	−46 ± 1	−45 ± 2
I−IV	120 ± 2	115 ± 1	120 ± 1	107 ± 2
II−III	−151 ± 4	−164 ± 2	149 ± 1	148 ± 2
II−IV	−45 ± 3	−45 ± 1	−40 ± 1	−46 ± 1
III−IV	162 ± 4	150 ± 2	−166 ± 1	−150 ± 1
I−I′	−152 ± 4	−144 ± 1	−153 ± 1	−165 ± 3
IV−IV′	153 ± 4	148 ± 1	155 ± 1	176 ± 2

[a] Interhelical angles (Ω) range from −180° to 180° and are classified as either parallel (∥) when 0° ≤ |Ω| ≤ 40° and 140° ≤ |Ω| ≤ 180° or as perpendicular (⊥) when 40° ≤ |Ω| ≤ 140° as described previously (*70*). [b] Interhelical angles for apo-mts1 were calculated using the computer programs Iha 1.4 and Interhlx. [c] Taken from the NMR structure (PDB entry 2CNP) of Mäler et al. (*23*). [d] Taken from the NMR structure (PDB entry 1B4C) of Drohat et al. (*25*). [e] Taken from NMR structure (PDB entry 1K2H) of Rustandi et al. (*27*).

Table 3: EF-Hand Angles of S100 Proteins Based on the VGM Method[a]

EF-hand	N-terminal coordinate of second helix	θ (deg)	ϕ (deg)
pseudo-EF-hand			
apo-mts1 EF1[a]	(12.043, −1.693, −3.188)	65 ± 2	102 ± 5
apocalcyclin EF1[a,b]	(9.885, 0.000, −4.697)	53 ± 2	101 ± 3
apo-S100B EF1[a,c]	(11.975, −3.434, −5.700)	55 ± 1	89 ± 4
apo-S100A1 EF1[a,d]	(13.128, −3.031, −4.793)	65 ± 4	88 ± 9
typical EF-hand			
apo-mts1 EF2[a]	(−13.307, 4.843, −2.210)	25 ± 4	−43 ± 13
apocalcyclin EF2[a,b]	(−12.870, 6.843, −0.710)	33 ± 2	−62 ± 4
apo-S100B EF2[a,c]	(13.128, −3.031, −4.793)	17 ± 1	−120 ± 4
apo-S100A1 EF2[a,d]	(4.417, 14.448, −0.288)	35 ± 2	−85 ± 7

[a] Vector geometry mapping (VGM) results were obtained using the program VGM as described previously (*71*). [b] Taken from the NMR structure (PDB entry 2CNP) of Mäler et al. (*23*). [c] Taken from the NMR structure (PDB entry 1B4C) of Drohat et al. (*25*). [d] Taken from the NMR structure (PDB entry 1K2H) of Rustandi et al. (*27*). The values for ω calculated by vgm for mts1 are 116° for EF1 and 332° for EF2. Apocalmodulin of Zhang et al. (PDB entry 1DMO) was used as the reference PDB compound (*78*).

two proposed S100 subfamilies (Figures 6 and 7). For example, Met-85 in helix 4 of mts1 is large, hydrophobic, and close to a relatively small amino acid residue, Ala-54, at the N-terminus of helix 3. The proximity of these two residues in the apo-mts1 structure is supported directly by a long-range NOE correlation observed between the methyl protons of Met-85 (M85ϵ) and Ala-54 (A54β; Figure 3B). It is likely that the large size of the Met-85 side chain critically affects the orientation of helix 3 relative to the other helices in mts1. A similar arrangement of helices is observed in the three-dimensional structure of apocalcyclin, which has a large hydrophobic residue (I83) at the position analogous to Met-85 of mts1 that packs into an alanine residue, Ala-51, at the N-terminus of helix 3.

For S100A1 and S100B, the position analogous to the large hydrophobic residue at the C-terminus of helix 4 in mts1 (M85) and calcyclin (I83) is occupied by a smaller alanine residue (i.e., A83 in S100B and A84 in S100A1; Table 4). These alanine residues are each nearby residues in the hinge of S100B (I47 and E49) and S100A1 (Q48 and D50). In the structures of S100B and S100A1, the location of the hinge is relatively well-defined and is supported by numerous NOE correlations (Table 4). In the case of S100B, packing of Ile-47 of the hinge into Ala-83 of helix 4 is likely an important determinant in the position of helix 3 of this protein (Figure 6). On the other hand, the analogous residues in the hinge of mts1 and calcyclin are charged (R49 in mts1 and K49 in calcyclin) and their packing into the hydrophobic patch at the C-terminus of helix 4 would be energetically unfavorable.

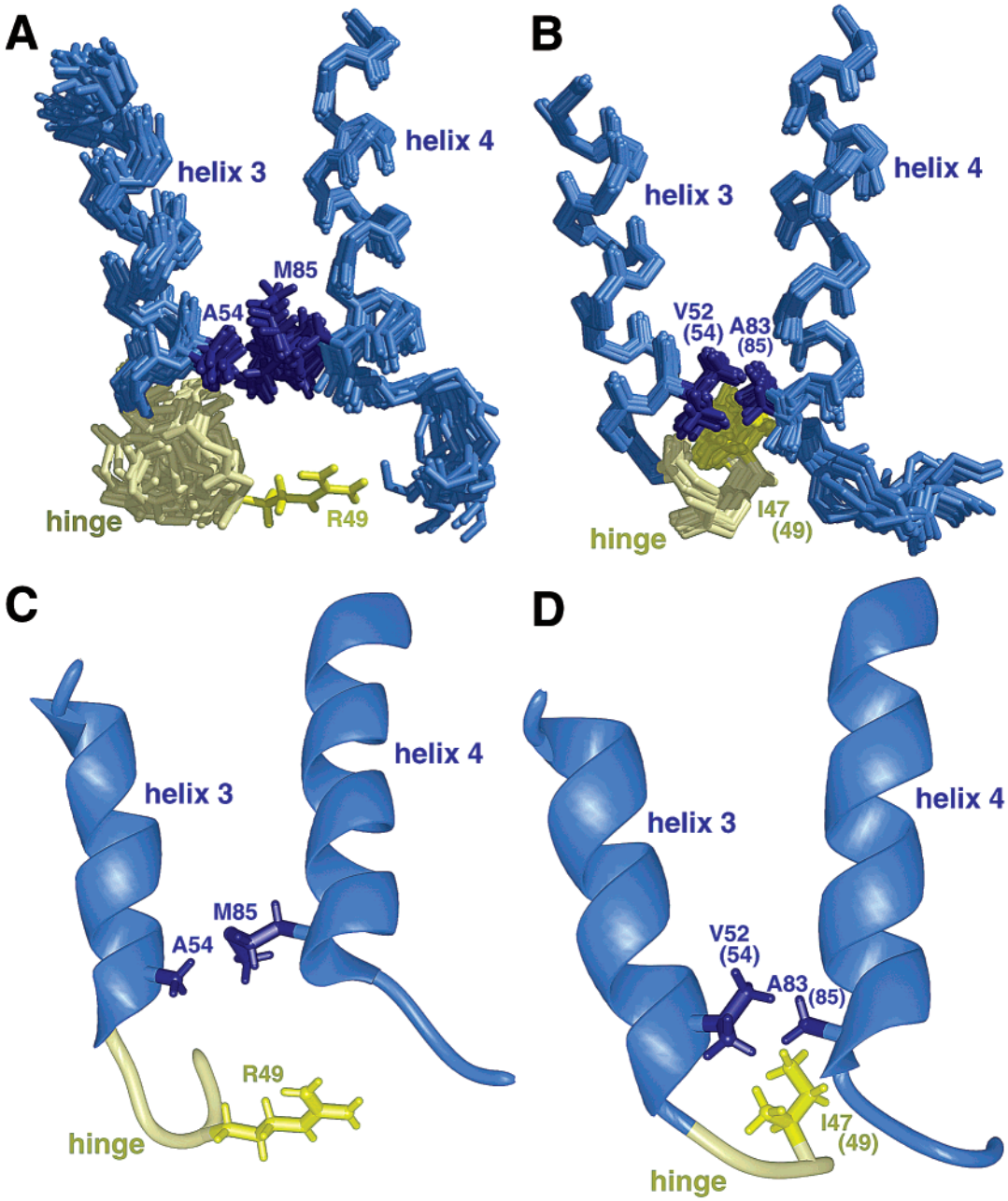

FIGURE 6: Comparison of side chain interactions for residues in the hinge and helix 4 of apo-mts1 (A and C) and apo-S100B (B and D). (A) Overlay of the 20 lowest-energy apo-mts1 structures (residues 47−64 and 72−89) with the side chains of Arg-49, Ala-54, and Met-85. For clarity, only the Arg-49 side chain closest to Met-85 and Ala-54 is shown. (B) Overlay of the 20 lowest-energy apo-S100B structures (residues 45−62 and 70−87) with the side chains and residues Ile-47, Val-52, and Ala-83. (C) Ribbon diagram of the hinge and helices 3 and 4 of apo-mts1. (D) Ribbon diagram of the hinge and helices 3 and 4 of apo-S100B. For S100B panels (B and D), corresponding mts1 residue numbers are included in parentheses.

Therefore, it is not surprising that NOE correlations between residues in the hinge and helix 4, as found in S100B and S100A1, are not observed for either mts1 or calcyclin in the apo state (Table 4). Thus, the position of the hinge relative to helix 4 represents another significant difference between the two proposed S100 subfamilies.

In summary, the amino acid sequences of S100B, S100A1, and several other S100 proteins (S100A5, S100A8, S100A9, S100A10, S100A11, S100A12, S100A14, Calg C, S100P, and S100Z) all have a small alanine side chain (or Thr for Calg C) at position 85 (using mts1 numbering) in the C-terminus of helix 4. For S100B and S100A1, this alanine residue on helix 4 is nearby residues in loop 2 (the hinge). On the other hand, large hydrophobic residues are at this position in mts1 (M85), calcyclin (I83), and two other S100 proteins (S100A2 and S100A3). In mts1 and calcyclin, these hydrophobic residues are proximal to an alanine residue in the N-terminus of helix 3, but are not nearby residues in the hinge. Therefore, on the basis of the sequence and structural data for these four apo-S100 proteins, predictions regarding other S100 proteins can be made (Table 5). For example, we predict that S100A2 and S100E will adopt helix 3−helix 4 interhelical angles in the apo state similar to that of mts1 and calcyclin, and that the remaining proteins in the S100 family (S100A5, S100A8, S100A9, S100A10, S100A11, S100A12, S100A14, Calg C, S100P, and S100Z) may adopt apo structures similar to those observed for S100B and S100A1 (Table 5). Two S100 proteins (S100A7 and S100A13)

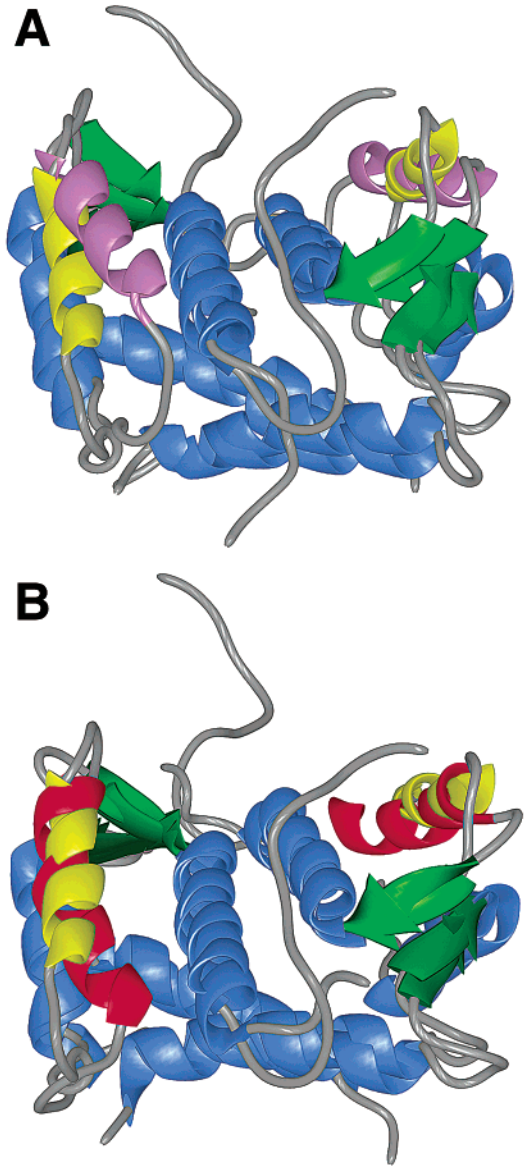

FIGURE 7: Ribbon diagrams comparing the three-dimensional structures of apo-mts1, apo-S100B, and apocalcyclin. (A) Overlay of apo-mts1 and apo-S100B with differences in the orientation of helix 3 shown in yellow (apo-mts1) and purple (apo-S100B). (B) Overlay of apo-mts1 and calcyclin with helix 3 of apo-mts1 (yellow) occupying a position similar to that found for calcyclin (red).

Table 4: Hinge−Helix 4 NOE Correlations

apo-mts1	apo-S100B[b]	apo-S100A1[c]
none observed[a]	$I47_{\gamma1} \rightarrow A83_{\beta}$	$Q48_{N} \rightarrow C85_{\alpha}$
	$I47_{\gamma2} \rightarrow A83_{\beta}$	$D50_{N} \rightarrow A84_{\beta}$
	$E49_{N} \rightarrow A83_{\beta}$	$D50_{\beta} \rightarrow A84_{\beta}$
		$D50_{\beta} \rightarrow A84\alpha$

[a] NOE correlations are also not observed between residues in the hinge and helix 4 in the data for apocalcyclin (PDB entry 1CNP) (*79*). [b] NOE data for S100B obtained from the NMR structure (PDB entry 1B4C) of Drohat et al. (*25*). [c] NOE data for S100A1 obtained from the NMR structure (PDB entry 1K2H) of Rustandi et al. (*27*).

could not easily be placed into either of the proposed S100 subfamilies. Nonetheless, the predictions for all of these S100 proteins will require validation via rigorous three-dimensional structure determinations in the apo state.

Ca^{2+}-Dependent Conformational Change. Consistent with a change in protein conformation, we and others (*72*) observe

Table 5: Proposed S100 Subfamilies[a]

	mts1 position 85	mts1 position 49
subfamily 1		
mts1 (A4)	M	R
S100L (A2)	M	K
S100E (A3)	Y	E
calcyclin (A6)	I	K
subfamily 2		
S100B	A	I
S100A1	A	Q
S100D (A5)	A	M
calgranulin A (A8)	A	−
calgranulin B (A9)	A	N
P11 (A10)	A	Q
S100C (A11)	A	Q
S100A12	A	−
S100A14	A	Q
calgranulin C	T	T
S100P	A	G
S100Z	A	Q

[a] Based on sequence alignment of several S100 family members (Figure 1) and structural data for apo-mts1, apocalcyclin, apo-S100A1, and apo-S100B. All members of the first subfamily of S100 proteins contain a residue with a large amino acid side chain at position 85 and a charged side chain at position 49 (using mts1 numbering). All S100 proteins in the second subfamily have an alanine at position 85 and a hydrophobic or neutral side chain at position 49 (using mts1 numbering). These differences in sequence affect the structure of S100 proteins with regard to the relative orientation of the hinge (loop 2), helix 3, and helix 4 (Figure 6; see the text). Psoriasin (A7) and S100A13 could not easily be assigned to either subfamily.

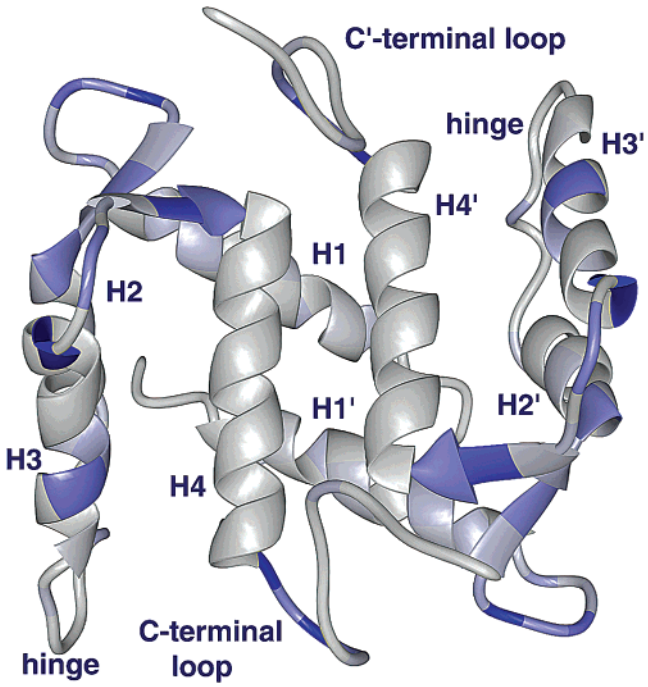

FIGURE 8: Ribbon diagram of apo-mts1 highlighting residues with significant ^{1}H and ^{15}N chemical shift perturbations upon addition of calcium. Similar chemical shift differences are derived from $^{15}N-^{1}H$ HSQC calcium titrations for human mts1 (this study) and for mouse mts1 reported elsewhere (*72*). The changes in chemical shift range from 0 (light gray) to 10 ppm (dark blue) and are color coded by changing the RGB value linearly to give a darker blue color for residues with larger changes in chemical shifts.

large perturbations in chemical shifts upon addition of Ca^{2+} to mts1 (Figure 8). It is likely that the conformational change in mts1 is similar to that observed for other S100 proteins since chemical shift perturbations for residues in the pseudo-

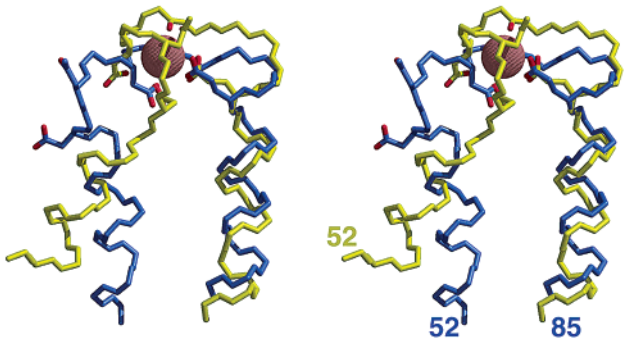

FIGURE 9: Overlay (in stereo) of the typical EF-hand from the apo-mts1 NMR structure and from a model of holo-mts1. The typical EF-hand is shown in blue for apo-mts1 and in yellow for the model of Ca^{2+}-bound mts1 (residues E52−M85).

EF-hand, the typical EF-hand, and other regions of the protein remote from the Ca^{2+}-binding domains such as in helix 3 and the C-terminal loop were observed (*24*, *73*−*75*). On the basis of these results, a preliminary homology-based model of holo-mts1 was calculated using the structures of holo-S100B, holocalcyclin, and holopsoriasin (Figure 9). It was found that regardless of which holo-S100 protein structure was used as the starting point in the calculation, the final model calculated for Ca^{2+}-bound mts1 was structurally very similar to holocalcyclin and less like the three-dimensional structure of holo-S100B or holopsoriasin (*24*, *73*−*77*). This was especially true with regard to the position of helix 3. However, the details of this conformational change still require a direct comparison of the high-resolution structure of mts1 in the Ca^{2+}-bound state **(**to be determined) to the three-dimensional structure of apo-mts1 determined here. Nonetheless, the Ca^{2+}-dependent binding of mts1 to its protein targets, such as myosin IIA, indicates that a conformational change is indeed necessary for mts1 function.

Summary. Multidimensional NMR techniques were used to determine the three-dimensional structure of apo-mts1 in solution. As with other S100 protein family members, mts1 is a symmetric homodimer with two EF-hand Ca^{2+}-binding domains per subunit. On the basis of chemical shift perturbations and the 3D structures of other holo-S100 proteins, it is anticipated that a calcium-dependent structural change will expose the target protein binding site in mts1. Furthermore, a comparison of the three-dimensional structure of apo-mts1 to other S100 proteins indicates that amino acid residues in these nonconserved regions (the hinge and C-terminal loop) affect the three-dimensional structure of S100 proteins in the apo state. For apo-mts1, its structure is more similar to that of apocalcyclin than it is to those of apo-S100A1 and apo-S100B. This difference in structure will likely impact the magnitude of the conformational change for mts1 upon addition of calcium and could be important for its biological function in vivo.

REFERENCES

1. Zimmer, D. B., Cornwall, E. H., Landar, A., and Song, W. (1995) *Brain Res. Bull. 37*, 417−429.
2. Donato, R. (2001) *Int. J. Biochem. Cell Biol. 33*, 637−668.
3. Donato, R. (1999) *Biochim. Biophys. Acta 1450*, 191−231.
4. Heizmann, C. W., and Cox, J. A. (1998) *Biometals 11*, 383−397.
5. Moore, B. (1965) *Biochem. Biophys. Res. Commun. 19*, 739−744.
6. Schafer, B. W., and Heizmann, C. W. (1996) *Trends Biochem. Sci. 21*, 134−140.
7. Ebralidze, A., Tulchinsky, E., Grigorian, M., Afanasyeva, A., Senin, V., Revazova, E., and Lukanidin, E. (1989) *Genes Dev. 3*, 1086−1093.
8. Nikitenko, L. L., Lloyd, B. H., Rudland, P. S., Fear, S., and Barraclough, R. (2000) *Int. J. Cancer 86*, 219−228.
9. Rudland, P. S., Platt-Higgins, A., Renshaw, C., West, C. R., Winstanley, J. H., Robertson, L., and Barraclough, R. (2000) *Cancer Res. 60*, 1595−1603.
10. Platt-Higgins, A. M., Renshaw, C. A., West, C. R., Winstanley, J. H., De Silva Rudland, S., Barraclough, R., and Rudland, P. S. (2000) *Int. J. Cancer 89*, 198−208.
11. Grigorian, M., Ambartsumian, N., Lykkesfeldt, A. E., Bastholm, L., Elling, F., Georgiev, G., and Lukanidin, E. (1996) *Int. J. Cancer 67*, 831−841.
12. Maelandsmo, G. M., Hovig, E., Skrede, M., Engebraaten, O., Florenes, V. A., Myklebost, O., Grigorian, M., Lukanidin, E., Scanlon, K. J., and Fodstad, O. (1996) *Cancer Res. 56*, 5490−5498.
13. Ambartsumian, N. S., Grigorian, M. S., Larsen, I. F., Karlstrom, O., Sidenius, N., Rygaard, J., Georgiev, G., and Lukanidin, E. (1996) *Oncogene 13*, 1621−1630.
14. Davies, M. P., Rudland, P. S., Robertson, L., Parry, E. W., Jolicoeur, P., and Barraclough, R. (1996) *Oncogene 13*, 1631−1637.
15. Watanabe, Y., Usada, N., Minami, H., Morita, T., Tsugane, S., Ishikawa, R., Kohama, K., Tomida, Y., and Hidaka, H. (1993) *FEBS Lett. 324*, 51−55.
16. Takenaga, K., Nakamura, Y., Sakiyama, S., Hasegawa, Y., Sato, K., and Endo, H. (1994) *J. Cell Biol. 124*, 757−768.
17. Kriajevska, M. V., Cardenas, M. N., Grigorian, M. S., Ambartsumian, N. S., Georgiev, G. P., and Lukanidin, E. M. (1994) *J. Biol. Chem. 269*, 19679−19682.
18. Grigorian, M., Andresen, S., Tulchinsky, E., Kriajevska, M., Carlberg, C., Kruse, C., Cohn, M., Ambartsumian, N., Christensen, A., Selivanova, G., and Lukanidin, E. (2001) *J. Biol. Chem. 276*, 22699−22708.
19. Strynadka, N. C. J., and James, M. N. G. (1989) *Annu. Rev. Biochem. 58*, 951−998.
20. Baudier, J., and Gerard, D. (1986) *J. Biol. Chem. 261*, 8204−8212.
21. Kligman, D., and Hilt, D. (1988) *Trends Biochem. Sci. 13*, 437−443.
22. Maler, L., Sastry, M., and Chazin, W. J. (2002) *J. Mol. Biol. 317*, 279−290.
23. Maler, L., Potts, B. C. M., and Chazin, W. J. (1999) *J. Biomol. NMR 13*, 233−247.
24. Drohat, A. C., Baldisseri, D. M., Rustandi, R. R., and Weber, D. J. (1998) *Biochemistry 37*, 2729−2740.
25. Drohat, A. C., Tjandra, N., Baldisseri, D. M., and Weber, D. J. (1999) *Protein Sci. 8*, 800−809.
26. Weber, D. J., Rustandi, R. R., Carrier, F., and Zimmer, D. B. (2000) *Interaction of dimeric S100B(ββ) with the tumor suppressor protein: A model for Ca-dependent S100-target protein interactions*, Kluwer Academic Publishers, Dordrecht, The Netherlands.
27. Rustandi, R. R., Baldisseri, D. M., Inman, K. G., Nizner, P., Hamilton, S. M., Landar, A., Zimmer, D. B., and Weber, D. J. (2002) *Biochemistry 41*, 788−796.
28. Drohat, A. C., Nenortas, E., Beckett, D., and Weber, D. J. (1997) *Protein Sci. 6*, 1577−1582.
29. Marion, D., Driscoll, P. C., Kay, L. E., Wingfield, P. T., Bax, A., Gronenborn, A. M., and Clore, G. M. (1989) *Biochemistry 28*, 6150−6156.
30. Bax, A., and Ikura, M. (1991) *J. Biomol. NMR 1*, 99−104.
31. Delaglio, F., Grzesiek, S., Vuister, G. W., Zhu, G., Pfeifer, J., and Bax, A. (1995) *J. Biomol. NMR 6*, 277−293.
32. Zhu, G., and Bax, A. (1992) *J. Magn. Reson. 98*, 192−199.
33. Zhu, G., and Bax, A. (1990) *J. Magn. Reson. 90*, 405−410.
34. Live, D. H., Davis, D. G., Agosta, W. C., and Cowburn, D. (1984) *J. Am. Chem. Soc. 106*, 1939−1941.
35. Spera, S., and Bax, A. (1991) *J. Am. Chem. Soc. 113*, 5490−5492.
36. Edison, A. S., Abilgaard, F., Westler, W. M., Mooberry, E. S., and Markley, J. L. (1994) *Methods Enzymol. 239*, 3−79.
37. Jeener, J., Meier, B. H., Bachmann, P., and Ernst, R. R. (1979) *J. Chem. Phys. 71*, 4546−4553.
38. Bax, A., and Davis, D. G. (1985) *J. Magn. Reson. 65*, 355−360.
39. Mori, S., Abeygunawardana, C., Johnson, M. O., and van Zijl, P. C. M. (1995) *J. Magn. Reson., Ser. B 108*, 94−98.

40. Kay, L. E., Marion, D., and Bax, A. (1989) *J. Magn. Reson. 84*, 72−84.
41. Marion, D., Ikura, M., Tschudin, R., and Bax, A. (1989) *J. Magn. Reson. 85*, 393−399.
42. Cavanagh, J., and Rance, M. (1992) *J. Magn. Reson. 96*, 670−678.
43. Ikura, M., Bax, A., Clore, G. M., and Groneborn, A. M. (1990) *J. Am. Chem. Soc. 112*, 9020−9022.
44. Vuister, G. W., Clore, G. M., Gronenborn, A. M., Powers, R., Garrett, D. S., Tschudin, R., and Bax, A. (1993) *J. Magn. Reson., Ser. B 101*, 210−213.
45. Kuboniwa, H., Grzesiek, S., Delaglio, F., and Bax, A. (1994) *J. Biomol. NMR 4*, 871−878.
46. Muhandiram, D. R., and Kay, L. E. (1994) *J. Magn. Reson., Ser. B 103*, 203−216.
47. Grzesiek, S., Anglister, J., and Bax, A. (1993) *J. Magn. Reson., Ser. B 101*, 114−119.
48. Grzesiek, S., and Bax, A. (1992) *J. Magn. Reson. 99*, 201−207.
49. Wittekind, M., and Mueller, L. (1993) *J. Magn. Reson., Ser. B 101*, 201−205.
50. Muhandiram, D. R., Guang, Y. X., and Kay, L. E. (1993) *J. Biomol. NMR 3*, 463−470.
51. Bax, A., and Pochapsky, S. S. (1992) *J. Magn. Reson. 99*, 638−643.
52. Clore, G. M., Nilges, M., Sukumaran, D. K., Brunger, A. T., Karplus, M., and Gronenborn, A. M. (1986) *EMBO J. 5*, 2729−2735.
53. Clore, G. M., Gronenborn, A. M., Nilges, M., and Ryan, C. A. (1987) *Biochemistry 26*, 8012−8013.
54. Wuthrich, K. (1986) *NMR of Proteins and Nucleic Acids*, John Wiley, New York.
55. Drohat, A. C., Amburgey, J. C., Abildgaard, F., Starich, M. R., Baldisseri, D., and Weber, D. J. (1996) *Biochemistry 35*, 11577−11588.
56. Wishart, D. S., and Sykes, B. D. (1994) *J. Biomol. NMR 4*, 171−180.
57. Brunger, A. T. (1992) *X-PLOR Version 3.1, A system for X-ray crystallography and NMR*, Yale University Press, New Haven, CT.
58. Nilges, M., Clore, G. M., and Gronenborn, A. M. (1988) *FEBS Lett. 229*, 317−324.
59. Nilges, M., Kuszewski, J., and Brunger, A. T. (1991) *Computational aspects of the study of biological macromolecules by NMR*, Plenum Press, New York.
60. Kuszewski, J., Nilges, M., and Brunger, A. T. (1992) *J. Biomol. NMR 2*, 33−56.
61. Nilges, M. (1993) *Proteins: Struct., Funct., Genet. 17*, 297−309.
62. Kuszewski, J., Gronenborn, A. M., and Clore, G. M. (1995) *J. Magn. Reson., Ser. B 107*, 293−297.
63. Kuszewski, J., Gronenborn, A. M., and Clore, G. M. (1996) *Protein Sci. 5*, 1067−1080.
64. Sali, A., and Blundell, T. L. (1993) *J. Mol. Biol. 234*, 779−815.
65. Fiser, A., Do, R. K., and Sali, A. (2000) *Protein Sci. 9*, 1753−1773.
66. Marti-Renom, M. A., Stuart, A. C., Fiser, A., Sanchez, R., Melo, F., and Sali, A. (2000) *Annu. Rev. Biophys. Biomol. Struct. 29*, 291−325.
67. Brünger, A. T. (1992) *XPLOR*, version 3.1, Yale University Press, New Haven, CT.
68. Rustandi, R., Vallely, K. M., Varlamova, O., Klein, M. G., Almo, S. C., Bresnick, A. R., and Weber, D. J. (2001) *J. Biomol. NMR 19*, 381−382.
69. Laskowski, R. A., MacArthur, M. W., Moss, D. S., and Thornton, J. M. (1993) *J. Appl. Crystallogr. 26*, 283−291.
70. Harris, N. L., Resnell, S. R., and Cohen, F. E. (1994) *J. Mol. Biol. 236*, 1356−1368.
71. Yap, K. L., Ames, J. B., Swindells, M. B., and Ikura, M. (1999) *Proteins 37*, 499−507.
72. Dutta, K., Cox, C. J., Huang, H., Basavappa, R., and Pascal, S. M. (2002) *Biochemistry 41*, 4239−4245.
73. Sastry, M., Ketchem, R. R., Crescenzi, O., Weber, C., Lubienski, M. J., Hidaka, H., and Chazin, W. J. (1998) *Structure 6*, 223−231.
74. Smith, S. P., and Shaw, G. S. (1998) *Biochem. Cell Biol. 76*, 324−333.
75. Smith, S. P., and Shaw, G. S. (1998) *Structure 6*, 211−222.
76. Brodersen, D. E., Etzerodt, M., Madsen, P., Celis, J. E., Thogersen, H. C., Nyborg, J., and Kjeldgaard, M. (1998) *Structure 6*, 477−489.
77. Brodersen, D. E., Nyborg, J., and Kjeldgaard, M. (1999) *Biochemistry 38*, 1695−1704.
78. Zhang, M., Tanaka, T., and Ikura, M. (1995) *Nat. Struct. Biol. 2*, 758−767.
79. Potts, B. C. M., Smith, J., Akke, M., Macke, T. J., Okazaki, K., Hidaka, H., Case, D. A., and Chazin, W. J. (1995) *Nat. Struct. Biol. 2*, 790−796.
80. Spera, S., and Bax, A. (1991) *J. Am. Chem. Soc. 113*, 5490−5492.
81. Wishart, D. S., Sykes, B. D., and Richards, F. M. (1991) *J. Mol. Biol. 222*, 311−333.
82. Wishart, D. S., Sykes, B. D., and Richards, F. M. (1992) *Biochemistry 31*, 1647−1651.

BI020365R